Nuclear magnetic resonance of ion implanted ^{8}Li in ZnO

Jonah R. Adelman,[1, *] Derek Fujimoto,[2, 3] Martin H. Dehn,[2, 3] Sarah R. Dunsiger,[4, 5] Victoria
L. Karner,[1, 2] C. D. Philip Levy,[4] Ruohong Li,[4] Iain McKenzie,[4] Ryan M. L. McFadden,[1, 2, †]
Gerald D. Morris,[4] Matthew R. Pearson,[4] Monika Stachura,[4] Edward Thoeng,[3, 4] John
O. Ticknor,[1, 2] Naoki Ohashi,[6] Kenji M. Kojima,[4] and W. Andrew MacFarlane[1, 2, 4, ‡]

[1]*Department of Chemistry, University of British Columbia, Vancouver, BC V6T 1Z1, Canada*
[2]*Stewart Blusson Quantum Matter Institute, University of British Columbia, Vancouver, BC V6T 1Z4, Canada*
[3]*Department of Physics and Astronomy, University of British Columbia, Vancouver, BC V6T 1Z1, Canada*
[4]*TRIUMF, 4004 Wesbrook Mall, Vancouver, BC V6T 2A3, Canada*
[5]*Department of Physics, Simon Fraser University, Burnaby, BC V5A 1S6, Canada*
[6]*National Institute for Materials Science (NIMS), 1-1 Namiki, Tsukuba 305-0044, Japan*
(Dated: September 20, 2021)

We report on the stability and magnetic state of ion implanted ^{8}Li in single crystals of the semiconductor ZnO using β-detected nuclear magnetic resonance. At ultradilute concentrations, the spectra reveal distinct Li sites from 7.6 to 400 K. Ionized shallow donor interstitial Li is stable across the entire temperature range, confirming its ability to self-compensate the acceptor character of its (Zn) substitutional counterpart. Above 300 K, spin-lattice relaxation indicates the onset of correlated local motion of interacting defects, and the spectra show a site change transition from disordered configurations to substitutional. Like the interstitial, the substitutional shows no resolved hyperfine splitting, indicating it is also fully ionized above 210 K. The electric field gradient at the interstitial ^{8}Li exhibits substantial temperature dependence with a power law typical of non-cubic metals.

I. INTRODUCTION

For many years the electronic properties of ZnO have held substantial practical appeal. It is a transparent wide bandgap (3.4 eV) semiconductor with a large exciton binding energy (60 meV) enabling potential room temperature optoelectronic applications.[1,2] It can be doped magnetically, either by replacing the nonmagnetic ($3d^{10}$) Zn^{2+} with a magnetic transition metal (or, more subtly, by intrinsic magnetic defects[3]) to produce a room temperature dilute magnetic semiconductor[4] useful in spintronics.[5] It also exhibits many interesting surface effects including photocatalysis, adsorbate sensitive photoconductivity,[6] and a photogenerated metallic state.[7] Key to realizing the potential of this remarkable range of properties is understanding and control of the point defects (both intrinsic and extrinsic) of its ideal hexagonal wurtzite structure.[8] Particularly, for p-type doping this has proven difficult,[9] but there are clear indications of progress in the production of LEDs[10] and even extremely high mobility epitaxial structures exhibiting the quantum Hall effect.[11]

Consistent and stable hole doping of ZnO is an important challenge that has remained the main barrier to implementation in optoelectronic devices. Substitution of divalent Zn for a monovalent alkali is an approach that has been studied in some detail.[1,8] While substitutional Li is an acceptor that compensates the natural n-type doping to some extent, this has not led to a reliable route to p-type ZnO. One reason for this is that Li is an amphoteric dopant: when interstitial it is a donor, so it can self-compensate. In addition to carrier doping, the magnetic aspect of Li defects is of interest for spin filtering.[3] In this context, detailed experimental charac-

terization of the structure, stability, and magnetic state of isolated Li defects would be very useful, particularly as a test of theoretical calculations.

To this end, we implanted a low energy (20-25 keV) beam of the shortlived radioisotope $^8Li^+$ into high purity single crystals of ZnO and studied the resulting isolated implant via its nuclear magnetic resonance as reported by its radioactive beta decay (β-NMR).[12] Closely related to muon spin rotation (μSR) which has yielded an intricate understanding of isolated hydrogen impurities in ZnO,[13,14] β-NMR enables complementary investigations of other light isotope dopants in II-VI semiconductors.[15,16] Our purpose is threefold: 1) to elucidate the properties of the Li dopant, 2) as a control for future experiments focusing on thin films and surface effects in pure and intentionally doped ZnO, and 3) as a first step towards studying more complex related materials, such as indium gallium zinc oxide (IGZO) used in thin-film transistors.[17] In the temperature (T) range of 7.6 to 400 K, we observe three distinct defects and a broad resonance originating from a distribution of metastable complexes. Density functional theory calculations of the electric field gradient (EFG) tensor, that determines the quadrupolar splitting of the NMR, support the assignment of (diamagnetic) defect configurations for the interstitial (Li_i^{O+}) and substitutional (Li_{Zn}^-). The interstitial is ionized and stable across the entire T range as a source of self-compensation, while the substitutional becomes prevalent only above 300 K as a shallow acceptor. We attribute spin-lattice relaxation above 300K to the onset of local defect dynamics. We observe a minor fraction of Li in a third characteristic site and discuss its possible origins. Finally, we report the temperature dependence of the EFG for the interstitial, which exhibits

a remarkable similarity to non-cubic metals.

II. EXPERIMENTAL

A. Implanted Ion β-NMR

In this form of β-NMR, we measure the NMR of a short-lived β-radioactive probe implanted into the crystalline host as a low energy ion beam. Detection uses the asymmetric β-decay (i.e. the direction of the emitted β electron is correlated to the nuclear spin direction at the instance of the decay), similar to μSR.[12] The experiments were performed at TRIUMF's ISAC facility in Vancouver, Canada, where a 20-25 keV beam of spin-polarized ^{8}Li$^+$ with an intensity of $\sim 10^6$ ions s^{-1} was focused into a beamspot ~ 2 mm in diameter centred on the sample. In this energy range, SRIM Monte Carlo simulations[18] predict a mean implantation depth ~ 100 nm (Appendix B). The ^{8}Li nuclear spin I is polarized in-flight using a collinear optical pumping scheme with circularly polarized light.[19] The beam is incident upon the sample centred in a high homogeneity superconducting solenoid producing a field $B_0 = 6.55$ T parallel to the beam and defining the z direction. The polarization p_z, the expectation value I_z divided by I, of the implanted ^{8}Li is monitored through the experimental β-decay asymmetry,

$$A(t) = \frac{N_F(t) - N_B(t)}{N_F(t) + N_B(t)} = a_0 p_z(t) \qquad (1)$$

where N_F and N_B are the β-rates in two opposing scintillation detectors downstream (Forward, F) and upstream (Backward, B) of the sample. a_0 is a proportionality constant depending on properties of both the decay and the detectors. The polarization direction is alternated, via the sense of circular polarization of the pumping light, between parallel and antiparallel with the beam ($\pm$ helicity), and data for each helicity is collected separately to enable accurate baseline determination, reduce systematic error, and to sometimes identify helicity dependent features. ^{8}Li has a nuclear spin $I = 2$, gyromagnetic ratio $\gamma/2\pi = 6.3016$ MHz T^{-1}, nuclear electric quadrupole moment of $Q = +32.6$ mb,[20] and mean radioactive lifetime $\tau = 1.21$ s. The short τ and a typical flux of $\sim 10^6$ ions s^{-1} ensures that the number of ^{8}Li in the sample is never higher than $\sim 10^7$, so the probe is ultradilute, and thus Li-Li interactions are absent. Further details on the measurements and samples are in section II C.

B. ^{8}Li NMR

Here we summarize the NMR properties of ^{8}Li that will be important in interpreting the results presented below.

Like its stable isotope counterparts, ^{8}Li is a quadrupolar nucleus with $I > 1/2$, meaning its nuclear charge distribution is not spherical, and its nuclear spin is thus coupled to the tensor electric field gradient (EFG) V_{ij} that it finds at its site in the crystal. The quadrupolar interaction splits the NMR spectrum into a multiplet of $2I = 4$ quadrupolar satellites, each corresponding to a specific $|\Delta m| = 1$ transition among adjacent nuclear magnetic sublevels indexed by m. Because I is an integer (rare among stable nuclei, but represented, for example, by the $I = 1$ ^{6}Li), there is no $m = \pm 1/2$ "main line" transition at the centre of the quadrupolar multiplet. The scale of the quadrupole splitting is given by the product of the EFG with the nuclear electric quadrupole moment eQ. We quantify it by defining the quadrupole frequency by

$$h\nu_q = \frac{3eQV_{zz}}{4I(2I - 1)} = \frac{eQV_{zz}}{8}, \qquad (2)$$

where V_{zz} is the (largest) principal component of the EFG. Typical of light nuclei, Q is not very large, and ν_q is typically on the kHz scale in close-packed crystals. One can then treat the quadrupolar interaction accurately as a first order perturbation on the Zeeman Hamiltonian, whereupon the satellites are distributed symmetrically about the NMR frequency ν_r with positions given by

$$\nu_i = \nu_r - n_i \nu_q \frac{1}{2}(3\cos^2\theta - 1 + \eta\sin^2\theta\cos 2\phi) \qquad (3)$$

where $n_i = \pm 1(\pm 3)$.[21] θ and ϕ are the polar and azimuthal angles of the field B_0 in the principal axis system of the EFG. The asymmetry parameter $\eta \in [0, 1]$ is a measure of the deviation of the EFG from axial symmetry ($\eta = 0$). If the site has threefold or higher symmetry, the EFG will be axial. If it is cubic, the EFG (and splitting) are zero.

To measure a resonance spectrum we use a transverse RF field (B_1) that induces magnetic dipolar transitions of $|\Delta m| = 1$. When the magnetic field of B_1 is large enough, we can, in some cases, also observe nonlinear multiquantum transitions (MQ), e.g. with $|\Delta m| = 2$. These resonances interlace the single quantum satellites with positions given by the same formula with $n_i = 0(\pm 2)$. Aside from being very strongly dependent on B_1, the multiquantum satellites are unaffected by a distribution of ν_q (quadrupolar broadening) resulting from crystal imperfections, so they are often noticably narrower than their single quantum counterparts.[22] We note that one major source of linewidth in solids, magnetic nuclear dipolar broadening, is nearly absent in ZnO, since the nuclear moments of Zn and O are small and/or low abundance. We thus expect the predominant broadening will be from crystalline disorder.

We will use the quadrupolar splitting as a fingerprint of the specific crystallographic site for the implanted ^{8}Li. Moreover, the EFG can be calculated accurately in density functional theory,[23–26] and we performed such calculations to aid in determining the sites, see section II D below.

Aside from the quadrupolar splitting, the NMR frequency ν_r is shifted from the Larmor frequency $\nu_0 = (\gamma/2\pi)B_0$ in the applied field by the magnetic response of the host. We quantify this shift by comparison to a standard reference. With the superconducting magnet in persistence mode, our conventional reference is a single crystal of cubic MgO, where the site is cubic, and the ^{8}Li NMR consists of a single narrow line.[27] We define the relative shift in parts per million (ppm) as

$$\delta = \frac{\nu_r - \nu_{\mathrm{MgO}}}{\nu_{\mathrm{MgO}}} \cdot 10^6. \qquad (4)$$

The resonance shift has contributions from the macroscopic demagnetization field, local magnetic fields of unpaired spins in the vicinity, and the local screening response, i.e. the chemical (orbital) shift.[12] The latter is well-known from stable Li NMR to exhibit a very small range of a few ppm; while the demagnetization field depends on the shape of the sample, and it is near its largest in our geometry: a thin plate in a perpendicular field.

In addition to the time average local fields that determine the spectral features, fluctuations of these fields at the NMR frequency determine the spin-lattice relaxation (SLR). Like conventional NMR, ^{8}Li relaxation is described by a relaxation function (recovery curve) typically parametrized by the rate $1/T_1$. The finite ^{8}Li lifetime τ limits measurable T_1 roughly to the range $0.01\tau < T_1 < 100\tau$. Because the spin is polarized in flight, no RF is needed to measure the relaxation, but as a result, there is no spectral resolution to the relaxation which is simply the average of all the ^{8}Li in the sample. The type of fluctuations giving rise to the observed SLR can often be determined by the characteristic temperature dependence of $1/T_1$. In a nonmagnetic insulating host, fluctuations may arise from stochastic diffusive motion of interstitial ^{8}Li or from lattice vibrations (phonons). In a semiconductor, mobile or localized carriers, if they are sufficiently abundant, may provide other sources for relaxation.[28]

C. β-NMR Measurements

We used two transparent colorless commercial hydrothermally grown ZnO single crystals (Tokyo Denpa Co. Ltd., Tokyo) in the form of thin plates $10 \times 8 \times 0.5$ mm^3 perpendicular to (0001), the hexagonal crystallographic c axis.[29] One sample was used "as-grown" (AG) while the other(n$^+$) was annealed at $1400\,^\circ$C to remove impurities. Typical AG carrier concentrations around room temperature are 10^{12} - 10^{15} cm^{-3}, while annealing raises it to 10^{16} - 10^{17} cm^{-3} by eliminating compensating defects (such as Li) residual from the growth process. Annealing was done prior to polishing and the polished surfaces had step-and-terrace structure with a typical step height $\sim 0.5 - 3$ nm. The same crystals were used for μSR experiments which showed a shallow muonium signal, typical of high quality ZnO. For the measurements,

the crystals were clamped to the Al sample holder of an ultra-high vacuum cold finger He flow cryostat.

With $B_0 = 6.55$ T parallel to the crystalline c-axis, we performed three types of measurement as a function of temperature. A) With a continuous beam, we measured the resonance spectrum by stepping the frequency of a continuous wave transverse RF magnetic field B_1 through the Larmor frequency. On-resonance, the RF causes the ^{8}Li spin to precess, decreasing the time integrated asymmetry.

B) A second type of resonance measurement was used in which the RF consisted of a four frequency comb with equal amplitude oscillations at frequencies determined by two parameters: $\tilde{\nu}_0$ and $\tilde{\nu}_q$. Specifically, at $\tilde{\nu}_0 \pm 3\tilde{\nu}_q$ and $\tilde{\nu}_0 \pm \tilde{\nu}_q$. The center $\tilde{\nu}_0$ was fixed at the resonance frequency from the normal spectrum described in A above, and the splitting parameter $\tilde{\nu}_q$ was then stepped through a range of values. The quadrupole satellites in the single mode RF spectrum suffer from small amplitudes, as a single transition is limited to at most 25% of the polarization. As a result, only a few spectra were obtained, which take considerable time to accumulate. In contrast, with the RF comb, when $\tilde{\nu}_q$ matches the quadrupole splitting, all the single quantum transitions ($\Delta m = 1$) can be saturated at once, dramatically increasing the amplitude, even revealing otherwise undetectable signals. The RF comb method has been previously applied to ^{12}B and ^{21}Na β-NMR in II-VI semiconductors and a more detailed description can be found elsewhere.[16,30,31]

Both types of resonance measurement differ in an important way from familiar conventional pulsed NMR, because the RF is applied continuously at each step of the scan for a relatively long integration time (1 s). In this mode, the resonance amplitudes are determined by several factors beyond the relative abundance of the corresponding ^{8}Li site. These include the RF amplitude B_1, the resonance linewidth, and, more subtly, slow dynamics of the resonance frequency on the integration timescale which can cause ^{8}Li spins to be double counted, since an individual spin need only be on-resonance for a millisecond or so during the integration time to be fully depolarized. As a result, it is difficult to make quantitative conclusions about site fractions from the amplitudes.

C) Measurements of the spin-lattice relaxation used a pulsed ^{8}Li$^+$ beam and no RF field. The time evolution of the polarization was measured both during and after the 4 second pulse. At its trailing edge, the polarization approaches a dynamic steady state, while after the pulse, it decays to its thermal equilibrium value near zero, giving rise to the characteristic bipartite NMR recovery curve. The helicity was alternated for each pulse every 20 seconds, and this process was repeated for about 30 minutes to accumulate statistics.

D. EFG Calculations

To facilitate site assignment for the implanted ^{8}Li, the EFG was calculated for various Li defect configurations using the supercell method. Here, Li is placed at a specific site in a supercell composed of a small number of ZnO unit cells which is then subjected to periodic boundary conditions. The calculation thus represents a fictitious ordered phase Li$_x$ZnO. While x in the calculation is vastly larger than in the experiment, by decreasing x to the extent possible, one can approach the dilute limit, particularly for quantities like the EFG that are predominantly sensitive to the immediate environment.[25,32,33]

Structural calculations of the defects were performed within the density functional theory framework using the plane wave pseudopotential method as implemented in Quantum Espresso.[34] Troullier-Martins norm-conserving pseudopotentials[35] were employed for treatment of core electrons and the generalized gradient approximation PBE was used for the exchange and correlation functional.[36] A supercell of $5a \times 5b \times 3c$ lattice units was used with a kinetic energy cutoff of 1080 eV and $2 \times 2 \times 2$ Monkhorst-Pack grid (MPG)[37] centred at the Γ point. The supercell had Li defects introduced at various sites with a compensating background jellium charge to maintain overall neutrality and avoid divergent Coulomb interactions. The atomic positions were allowed to fully relax under the constraint of fixed experimental lattice parameters.[38] The total energy was numerically converged to less than 1 meV with respect to a cutoff of 1210 eV and $6 \times 6 \times 6$ MPG.

For an isolated implanted Li$^+$, the surrounding ZnO lattice will respond with a localized distortion about the defect that leaves the more distant structure unchanged. The EFG has an r^{-3} dependence on distance and is thus very sensitive to the local structure, so a realistic calculation requires both the experimental lattice parameters and an accurate estimate of the local lattice relaxation.[25]

EFG calculations were performed using the more computationally expensive all-electron augmented plane wave plus local orbitals method (APW+lo) implemented in WIEN2k[39] and the relaxed structure from the pseudopotential method. The angular momentum expansion of the lattice harmonics inside the atomic spheres was truncated at $L = 10$ and the plane waves outside the atomic spheres expanded with a cutoff of $R_{MT}K_{Max} = 8$, the product of the smallest atomic sphere (R_{MT}) with the largest K-vector (K_{Max}) of the plane wave expansion.

III. RESULTS AND ANALYSIS

A. Resonance Spectra

Fig. 1 shows the single tone frequency spectrum in ZnO at three temperatures. At all temperatures, the primary feature is a quadrupolar multiplet pattern spread ± 45 kHz about its center. At 300 K, the predominant
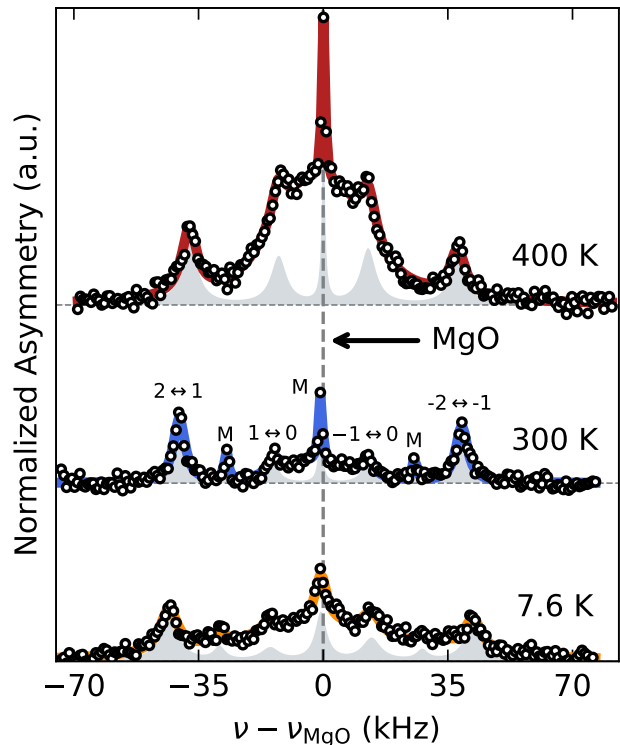

FIG. 1. The quadrupole split single tone RF spectra at several temperatures for ^{8}Li in the as-grown ZnO single crystal with 6.55 T$\| c$. The frequency scale is relative to the MgO calibration frequency (dashed line). The vertical scale has been normalized by the off-resonance asymmetry at each temperature, and the spectra are vertically offset for clarity. At 300 K, the single quantum satellites are labelled with their corresponding m values, and multiquantum with M. The fitted A site spectrum is shaded grey and is the dominant feature. Above 300 K, a second unresolved line (site B) emerges.

quadrupolar splitting is indexed by the corresponding magnetic sub-level transition. In addition to the indexed single quantum satellites (SQ), there are interlaced multi-quantum lines labeled M that are substantially narrower than their SQ counterparts.

The quadrupole splitting is expected, since no site in the wurtzite lattice is cubic. However, its magnitude (e.g. defined by the difference between the outermost satellites) is quite modest, $\sim 10\times$ smaller than in perovskite oxides.[40] The resolved multiplet indicates a well-defined crystalline site, which we label "A". The A multiplet is conspicuous at all temperatures, but its features evolve, with increased splitting and substantial broadening at low T. At the lowest temperature, the multiplet is superimposed on a broad pedestal of intensity with a width comparable to the overall multiplet splitting. In addition to A, at 300 K and above, there is another unresolved line close to the Larmor frequency (see the 400 K spectrum in Fig. 1). The helicity-resolved spectra confirm it to be

quadrupolar but with a substantially smaller splitting, such that the individual satellites are not resolved (see Appendix C). We conclude this corresponds to a second $^8Li^+$ site (B), with a much smaller EFG, whose population grows at high temperature.

To quantify these observations, the data was fit using a custom python code based on the Minuit2 library.[41,42] At each temperature, the two helicities were fit simultaneously sharing the parameters that determine the satellite positions. Note that for A, $\nu_q/\nu_r \sim 3 \times 10^{-4}$, so Eq. (3) provides the satellite positions very accurately. The fit function thus consisted of 7 Lorentzians with satellite positions determined by the single parameter ν_q via Eq. (3), assuming the c-axis coincides with the principal EFG direction ($\theta = 0$) and axial symmetry ($\eta = 0$). We discuss the validity of these assumptions below. It was further constrained by assuming all the SQ (MQ) satellites shared the same width $\Delta\nu_S$ ($\Delta\nu_M$) at each temperature. Where necessary, signals corresponding to the low T pedestal and the unresolved B site signal were added. *A priori* we expect the chemical shift at A and B will differ, but any such difference is too small to detect, and to reduce the number of parameters, the broad lines were centred at the same ν_r as A. The resulting fits are shown as the lines in Fig. 1, and the shared parameters for A are given in Table I.

The resulting ν_q, determined by the splittings, are quite precise, and the differences in Table I are significant as confirmed below by the comb spectra. We include the raw relative shift defined by Eq. (4) in Table I. From the sample shape, we estimate the dimensionless demagnetization factor is $N \approx 0.92$. A literature[43] value for the volume susceptibility of ZnO $\chi_v \approx -2.2 \times 10^{-6}$ leads to an estimated demagnetization shift $-4\pi(N - 1/3)\chi_v \approx$ 16 ppm, comparable to the value in the MgO reference crystal (~ 12 ppm[27]). From this, we conclude an accurate estimate of the corrected shift is impractical. However, the chemical shifts in MgO and ZnO are evidently small (a few ppm) and similar, consistent with expectations from conventional Li NMR. The reported shift uncertainties in Table I are purely statistical. Unlike the splitting, we do not regard the differences in the shift as significant, because it is sensitive to small systematic changes in the field at the sample, due to thermal contraction, weak magnetization of the spectrometer, and reproducibility of the sample position.

The annealed sample was measured briefly at 300 K (not shown). The SQ and MQ satellite linewidths at 300 K in the two samples are similar, while any difference in the quadrupole splitting is much smaller than the MQ linewidths and indistinguishable in a single tone spectrum.

In the AG sample, both the SQ and MQ satellites broaden significantly, and by a similar amount, at low temperature, indicating predominantly magnetic, rather than quadrupolar, broadening. Interestingly, the SQ satellites also broaden at high temperature above 300 K. The $n_i = \pm 2$ MQ satellites were not observed at 400 K,

so no comparison of their widths can be made.

Aside from the A multiplet, the broad lines are considerably less well-determined. The low temperature pedestal is very similar in the two helicities, meaning it shows little evidence of a resolved quadrupole splitting - or any such splitting is much less than the width which is on the order of 50 kHz FWHM. Without resolved satellites, it is not possible to reliably extract the quadrupolar splitting of the B site. From the helicity resolved fits, we estimate a splitting of at most a few kHz with satellite linewidths several times larger than this.
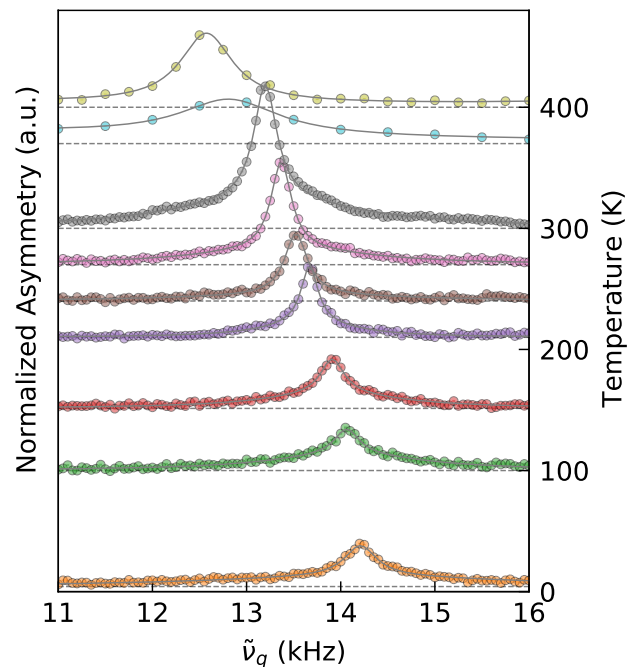
B. Comb Spectra

FIG. 2. The RF comb spectra, for a narrow range around ν_q for site A, as a function of temperature. The spectra are vertically offset by an amount proportional to the temperature. There is a clear reduction of ν_q with increasing T. The solid grey lines are bi-Lorentzian fits. Up to 300 K, the amplitude increases. Above this, there is a dramatic decrease and extensive broadening.

We turn now to the RF comb spectra that reveal more detail than the single frequency spectra above. Recall the central frequency of the comb is set to coincide with the centre of the multiplets in Fig. 1 and then the comb splitting is stepped over a range. When the comb's splitting parameter $\tilde{\nu}_q$ matches ν_q, we find a single resonance much larger than any of the individual satellites. This is demonstrated for the A site multiplet as a function of temperature in Fig. 2. The resonant $\tilde{\nu}_q$ is entirely

TABLE I. The shared best fit parameters for the A multiplet, including values for the quadrupole frequency ν_q, frequency shift δ, single quantum linewidths $\Delta\nu_S$, and multiquantum linewidths $\Delta\nu_M$ for both AG and n^+ samples. The errors in parentheses are purely statistical.

Sample	Temperature (K)	ν_q(kHz)	δ(ppm)	$\Delta\nu_S$(kHz)	$\Delta\nu_M$(kHz)
AG	7.6	14.23(2)	9.3(1)	6.0(4)	4(1)
AG	300	13.22(1)	5.9(7)	3.9(3)	1.2(2)
AG	400	12.56(2)	1.7(5)	5.2(2)	1.08(5)
n^+	300	13.16(1)	1.0(6)	3.9(1)	1.38(6)

consistent with the splitting in Fig. 1. With increasing temperature, the resonance position moves systematically downward, confirming the trend in Table I and revealing a thermal reduction in EFG which we discuss below in section IV D. The spectra could not be fit with a single Lorentzian, but required a bi-Lorentzian (narrow plus broad) sharing the same ν_q. The fit parameters, as a function of temperature, are shown as the triangles in Fig. 4. The resonance position provides a very accurate measurement of $\nu_q(T)$. The amplitude increases with increasing T, reaching a maximum at ~ 300 K, while it is widest at 370 K, consistent with the high temperature broadening of the SQ satellites in Table I.

For only a few high temperatures, we extended the $\tilde{\nu}_q$ scan range down to zero comb splitting. These spectra, shown in Fig. 3, reveal further structure. Distinct well defined quadrupole splittings for $\tilde{\nu}_q = \nu_q$ resonances are denoted by the vertical colored bands, with the grey band corresponding to the A resonance tracked with T in Fig. 2. In scanning $\tilde{\nu}_q$ over a wider range, it is important to recognize that when the outer(inner) comb frequencies match the inner(outer) SQ satellites of the underlying multiplet, we expect small aliased resonances at $\tilde{\nu}_q = \nu_q/3$ (and $3\nu_q$). These SQ resonances are denoted at 400 K by subscripts. There may also be aliased MQ resonances at $2\nu_q/3$ and $2\nu_q$. Scans of $\tilde{\nu}_q$ up to 82, 110 kHz at 300 and 400 K (not shown) reveal no further resonances with larger ν_q. The features at lower frequency includes a resolved resonance corresponding to the B site (shaded orange), with $\nu_q = 5.941(4)$ kHz at 400 K, and fit values as open squares in Fig. 4. This resonance is also identifiable at 210 K (not shown), indicating a small population of site B far below where it becomes evident in the single frequency spectra. The B resonance is also broader than A, and its position shifts higher from 370 to 400 K opposite to the reduction shown by A.

As discussed in section II C, the resonance amplitudes are determined by several factors, including the long integration time (1 s) of the continuously applied RF field and off-resonance baseline asymmetry. In the presence of slow spectral dynamics up to the integration time, the amplitude may be enhanced as ^{8}Li can be double counted if they only transiently meet the resonance condition for a time as short as the RF precession period, on the order of 1 ms. This results in spectra with resonance amplitudes whose sum may exceed the full off-resonance asymmetry,
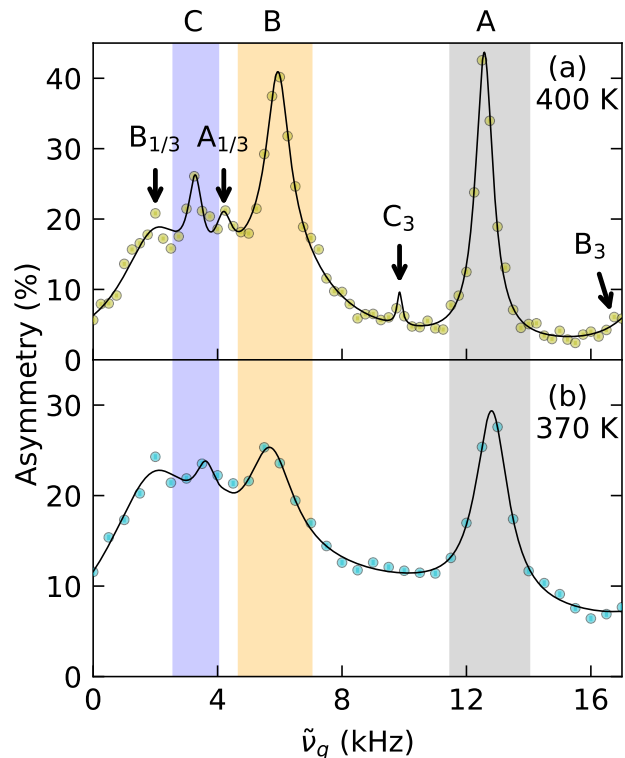

FIG. 3. The RF comb spectra for a broader range down to $\tilde{\nu}_q = 0$ at 400 K (a) and 370 K (b). Primary resonances for distinct sites are indicated with shaded regions, labelled A,B,C. The asymmetry has been normalized to its fitted off-resonance value. At 370 K, the lines are all broadened. Smaller features denoted as subscripted labels are aliases of the primary resonances. There is also a substantial broad background.

as is evidently the case in Fig. 3. This is strong confirmation that ^{8}Li is undergoing spectral dynamics in this temperature range.

The comb spectrum also reveals a third site (labelled C) with an even smaller $\nu_q = 3.63(5)$ kHz at 370 K, about half the value for B, decreasing to 3.28(5) kHz at 400 K. It's amplitude is small, so it corresponds to only a minor population of implanted ^{8}Li. The combination of the breadth of B and the presence of C explains the absence of resolved structure of the B line in Fig. 1, but note there

is substantial intensity in a broad background encompassing B and C with a tail that reaches toward A. The three resolved quadrupole frequencies at 400 K are given in Table II and the additional minor peaks are aliases of these resonances. The rich detail in these spectra demonstrates the power of the comb method to strongly amplify quadrupolar split resonances within a narrow band of $\tilde{\nu}_q$ and reveal structure that is otherwise hidden.

TABLE II. Measured quadrupole frequency ν_q and principal component of the EFG tensor V_{zz} for the three ^{8}Li sites at 400 K. Parenthetical values are statistical errors.

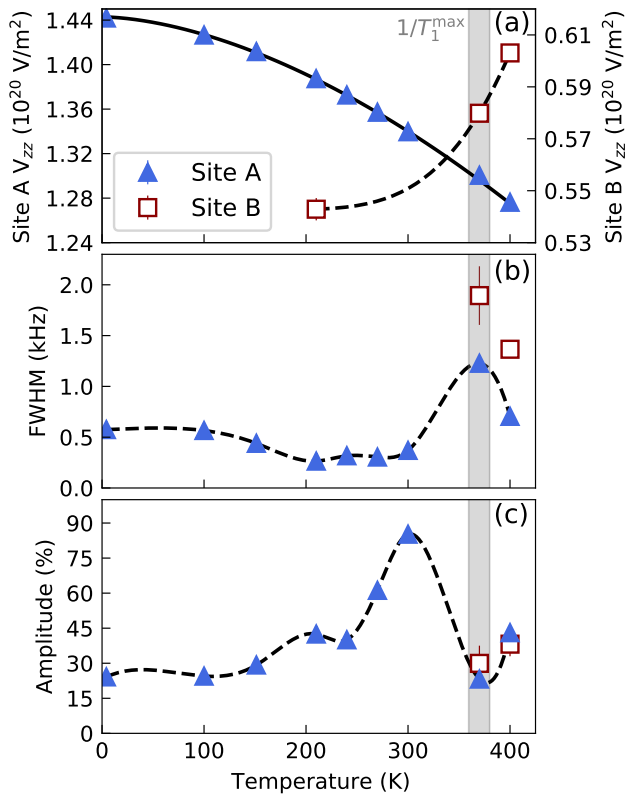| Site	ν_q(kHz)	$V_{zz}(10^{20}\text{V/m}^2)$
A	12.56(2)	1.275(2)
B	5.941(4)	0.6029(4)
C	3.28(5)	0.333(5)

FIG. 4. Temperature dependence of the fit parameters for the comb spectra in Figs. 2, 3. (a) From the resonance positions, the principal component of the EFG for sites A and B calculated using Eq. 3. (b) the linewidth (FWHM) for the bi-Lorentzian. (c) the resonance amplitude. The lines are guides to the eye, except the solid line in (a) is a fit to Eq. 6 for site A. The vertical band marks the position of the peak of the spin-lattice relaxation rate.
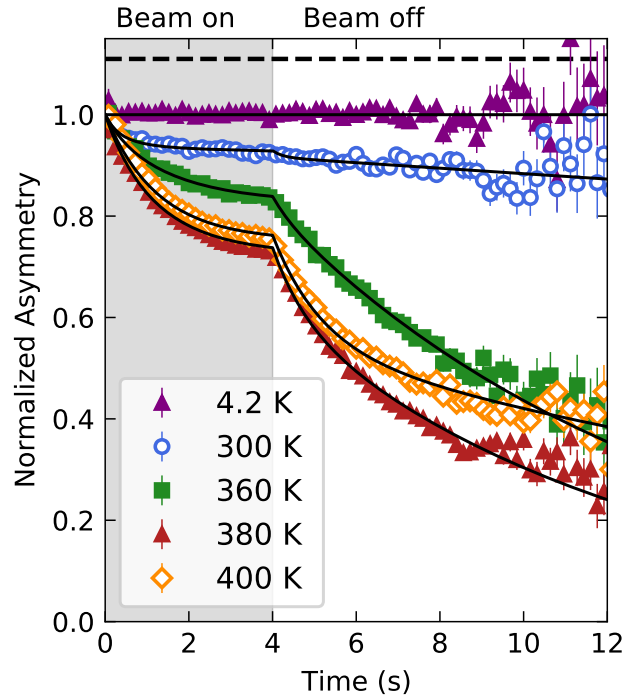
C. Spin-Lattice Relaxation

FIG. 5. The time dependence of the asymmetry for ^{8}Li$^+$ in the as-grown ZnO at 6.55 Tesla$\|$ c for several temperatures. The decay is due to spin-lattice relaxation of the isolated implanted ^{8}Li$^+$. The black lines are global fits with a biexponential relaxation function Eq. (5). Above 300 K, there is a strong temperature dependence with a maximum rate near 370 K. The dashed line shows the calibrated value of A_0 in MgO exceeds that in ZnO indicating a small missing fraction.

Below 300 K, the spin-lattice relaxation in the AG sample is very slow ($T_1 > 100$ s), as seen in the recovery curves in Fig. 5, where the time dependent asymmetry has been normalized to its initial value A_0. The corresponding rate is near the limit imposed by the ^{8}Li lifetime. This is typical for a nonmagnetic insulator when ^{8}Li$^+$ is not diffusing. However, above 300 K it increases rapidly, but not monotonically, with a maximum rate at about 370 K (the lowest data in Fig. 6). Careful comparison between 300 K and low temperature shows there is a small much faster relaxing component, corresponding to at most a few % of the signal. In addition, a calibration of the initial asymmetry A_0 in MgO is about 10% larger at 300 K, see the dashed horizontal line Fig. 5. Thus, there appears to be a small "missing fraction" corresponding to a population of ^{8}Li that are very rapidly depolarized.

We briefly studied the n^+ sample at 300 K and found the SLR rates to be similar. However, A_0 was larger, only 3.3(1)% less than MgO (see Fig. 11 in Appendix D), i.e. the missing fraction is substantially reduced by annealing.

To fit the data consistently across the full temperature range, we adopt a biexponential relaxation function: for ^{8}Li arriving at time t', the polarization at time $t > t'$ follows

$$R(t,t') = [f_s e^{-\lambda_s(t-t')} + (1-f_s)e^{-\lambda_f(t-t')}] \quad (5)$$

where f_s is the slow fraction and $\lambda_s = 1/T_1^{\text{slow}}$ is its rate, while λ_f is the fast SLR rate. The data was fit to Eq. (5) convolved with the 4 second beam pulse using the Minuit2[41,42] library as implemented in ROOT[44] with a custom C++ code. To reduce the number of free parameters, below 300 K $A_0 = 0.07822(5)$ and $f_s = 0.962(1)$ were shared temperature independent global parameters, and the global reduced $\chi^2 \sim 0.85$. The data above 300 K was taken after the spectrometer had been modified to increase its maximum temperature. For this data, f_s was allowed to vary with temperature and the shared $A_0 = 0.0854(2)$ with $\chi^2 = 0.87$. This increase in A_0 is due to changes to the F β-detector. In both ranges, the χ^2 values indicate the biexponential tends to overparametrize the data (particularly at low temperature); however, it has the advantage that it isolates the fast component, preventing it from biasing the slow rate. The rate and fraction of the large, slow-relaxing signal are presented in Fig. 6 showing the rapid increase in λ_s above 250 K toward a maximum at 370 ± 10 K. The fast signal is a very small fraction below 300 K, see Appendix A for more details.

D. EFG calculations

As the EFG is a ground state property of the charge density which is accessible within all-electron self-consistent energy band calculations,[23] we attempted to determine the site of ^{8}Li by comparison with the calculated EFG tensor magnitude and symmetry. In semiconductors, defects generally exhibit distinct charge states, and the lowest energy charge state may change with temperature (or doping) by exchanging electrons with band states at the Fermi level. Naturally, different charge states have different local lattice and electronic structures.[45] This modifies the EFG, allowing, in principle, identification of charge states, particularly for deep level defects characterized by large lattice relaxation at a charge state transition.[32,33] We indicate the charge state of the calculation with a superscript q, where $q = -1(+1)$ if an electron is added to (removed from) the supercell.

There are only a few reasonable candidate Li sites in ideal ZnO, with structure shown in Fig. 7. We calculate the defect structures for Li^+ in the high symmetry tetrahedral Li_T (Wykoff 2b) and octahedral $\text{Li}_\text{i}^\text{O}$ (Wykoff 2a) interstitial sites, where it would act as an electronic donor. We also calculate the zinc substitutional site (Li_Zn), an established acceptor.[46] Note that neutral Li_Zn has a polaronic distortion around the localized hole, so it is not certain whether it is a shallow (and potentially
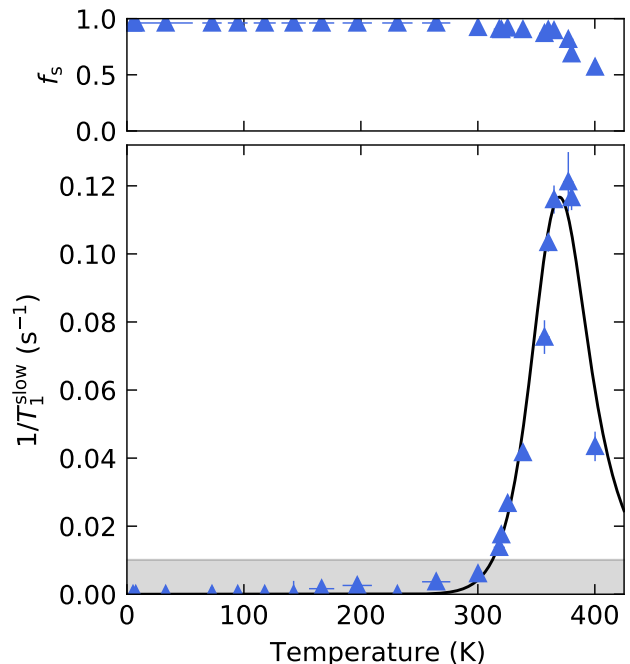

FIG. 6. The spin-lattice relaxation rate, $\lambda_s = 1/T_1^{\text{slow}}$ and fraction f_s for the large slow relaxing component from biexponential fits as shown in Fig. 5. Near 400 K, f_s decreases as more of the signal is accounted for by the fast component. There is a clear maximum at 370 K. The line is a fit to an activated BPP temperature dependence as described in the text. The grey region denotes the lower limit at which $1/T_1$ is accurately measured.

TABLE III. The electric field gradient V_{zz} in units of 10^{20} V/m^2 for selected relaxed Li defect configurations using the 300 K ZnO lattice parameters.

Site	V_{zz}	Principal Axes	η
$\text{Li}_\text{i}^\text{O+}$	1.21	(0,0,1)	0
$\text{Li}_\text{T}^{\star+}$	0.47	(0.04,0.82,-0.57)	0.65
Li_Zn^-	0.16	(0,0,1)	0

useful) p-type dopant.[47,48] The Li antisite defect (Li_O) is not considered, as it is reported to be unstable.[48]

We find $\text{Li}_\text{i}^\text{O+}$ is displaced from the symmetric 2a position along (0001) by 0.57 Å, creating a long and short set of Li-O coordinating bonds. The axially symmetric Li_T^+ is also found to relax spontaneously to $\text{Li}_\text{T}^{\star+}$, a variant displaced from the 3-fold axis of symmetry. Considering the defects only in their diamagnetic ionized states, the EFG tensors, calculated using the 300 K lattice parameters are given in Table III. The Li_Zn^- center distorts the local environment, giving rise to an almost symmetric tetrahedral coordination with neighboring oxygens, resulting in a very small V_{zz}. $\text{Li}_\text{i}^\text{O+}$ retains axial symmetry (along c), while $\text{Li}_\text{T}^{\star+}$ has a principal axis almost orthog-

onal to c, nearly parallel to b. The calculated structures of the Li_i^{O+} and Li_{Zn}^- defects are shown in Fig. 7.
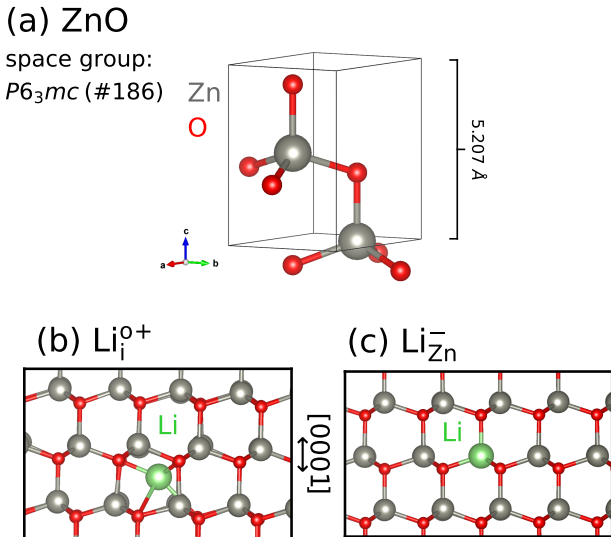

(a) ZnO

space group:
$P6_3mc$ (#186)

(b) Li_i^{o+} (c) Li_{Zn}^-

FIG. 7. Unit cell of ZnO (a) and the relaxed defects of Li_i^{O+} (b) and Li_{Zn}^- (c) in their diamagnetic states shown $\parallel c$ and $\perp b$. The off-center Li_i^{O+} is located at the $2a$ site with fractional coordinates $(0,0,0.079)$ of the unit cell shown. The structures were drawn using VESTA.[49]

IV. DISCUSSION

A. Sites for Implanted Li^+

When an ion is implanted in a crystal, it loses energy through collisions with host lattice atoms and gradually slows down. In the process, it can knock a host atom out of its normal lattice position into a nearby vacant interstitial site, forming a Frenkel (vacancy-interstitial) pair.[50] The threshold for this process is typically 10s of eV. So, after generating its final Frenkel pair, the implanted ion continues for some distance before stopping typically at a high symmetry site. The host lattice will then relax around the stopped implant, possibly lowering its site symmetry. Now if we consider the NMR spectrum, such as we measure with β-NMR, to the extent that the stopping site is isolated from other defects, it will have a characteristic EFG tensor reflected by a well-resolved quadrupolar splitting. However, it is also possible that the ion stops close enough to the last Frenkel pair that its EFG is modified. As there are many possible configurations of the trio (ion+pair), this results in a distribution of EFGs and is reflected in a quadrupolar broadened resonance usually observed at low temperature. At higher T, the Frenkel defects tend to heal rapidly, typically leading to the first stage of annealing.

Depending on relative mobilities, the implanted ion may compete for the vacancy with the intrinsic interstitial of the pair. With increasing T, the typical behaviour is thus a gradual loss of the broad "perturbed site" resonance together with an increase and sharpening of the well-defined lines corresponding to the isolated site, and potentially (if the implant reaches the vacancy) a change of site to substitutional. As we shall see below, the implanted $^8Li^+$ in ZnO follows this phenomenology quite closely.

The A site multiplet, with a well-resolved quadrupolar splitting, is evident at all temperatures, including the lowest, see Fig. 1, so it should correspond to $^8Li^+$ at the most stable interstitial. The octahedral site is substantially more spacious than the tetrahedral, and theory finds it lower in energy by 0.62 eV.[47] Moreover, there is only a small barrier for the tetrahedral to migrate to an adjacent octahedral.[47] The Li_i^{O+} assignment is unambiguously confirmed by the excellent agreement between the calculated EFG of $1.21 \cdot 10^{20}$ V/m^2 in Table III with the experimental value at room temperature of $1.342(1) \cdot 10^{20}$ V/m^2. The unrelaxed $2a$ site is symmetrically coordinated by six O^{2-} ions. Axial lattice relaxation brings the interstitial cation closer to three anions, lowering the energy. This off-centre site is also consistent with emission channeling from other alkali radioisotopes in wurtzite crystals.[51–53] We note the relaxed site is still 3-fold symmetric about the c axis, so the EFG remains axial, consistent with Eq. (3) for the satellite splittings. As a corollary, we then attribute the broad low temperature resonance in Fig. 1 that disappears by 300 K to Li_i^{O+} in the vicinity of some implantation-related crystalline disorder, also consistent with emission channeling in related materials.[53]

Next we consider the B site resonance which is well-resolved only in the comb spectra. Though it can be identified as low as 210 K, it only becomes substantial above 300 K, increasing in amplitude towards the highest T. This suggests B is the product of a site change transition to a lower energy site, likely the substitutional. This is similar to ^{24}Na implanted into ZnO where emission channeling finds the interstitial twice as probable as the substitutional at room temperature, while by 420 K the interstitial is largely converted to substitutional.[51] In contrast to the A site, the calculated EFG is substantially smaller than measured. However, Na β-NMR also finds two sites at room temperature, with the substitutional site having a factor of 2 smaller EFG than the interstitial,[30,51] very similar to ^8Li. The evident underprediction of the EFG by DFT (see Table III) is probably due to its sensitivity to the detailed lattice relaxation around the Li_{Zn}^- which may not be captured accurately with the GGA functional.

The temperature dependence of the spectra reveals further aspects of the site change. The A site line (most clearly revealed in the comb resonances in Fig. 2) increases in amplitude above 200 K, reaching a maximum near room temperature. Some of this increase is due to

narrowing. The bi-Lorentzian lineshape also suggests two A sites sharing the same average EFG, but distinguished by the width of the EFG distribution. The broad component probably corresponds to the A site with some disorder at distances of a few lattice constants, while the narrow component probably represents an A site with ideal local structure. The growth of the narrow component is consistent with annealing of some correlated (small) Frenkel pairs in the vicinity. This agrees with optically detected electron paramagnetic resonance in electron irradiated ZnO that demonstrates low temperature annealing of the zinc (65-170 K) and oxide (160-230 K) sublattices.[54] As seen clearly in Fig. 3, above 300 K, the A line first broadens at 370 K, then narrows again by 400 K, maintaining nearly the same integrated area, while B increases substantially. If the site change involved an isolated interstitial becoming substitutional, e.g. by a knock out mechanism,[55] then we would expect a decrease in the A amplitude with the simultaneous growth of B, such as in the well-established site change in the FCC metals.[56] This is not the case, however. While it is possible that dynamic effects on the amplitude are confounding here, a careful inspection of the spectra in Fig. 3 reveals that the increase in B appears to be at the expense of the very broad background intensity that underlies the better resolved resonances. Production of Li_{Zn}^{-} in this T range then appears to result from a perturbed (disordered) site as a starting point rather than the isolated interstitial directly. This is reasonable for a site change involving a nearby vacancy (which is almost certainly implantation-related, since thermodynamic vacancies are extremely rare). Interstitials nearest to such vacancies will be the first to become substitutional, and they will also experience a significantly perturbed EFG in advance of the site change. In the ideal crystal, the barrier for Zn vacancy migration is quite high,[57] so the site change is probably driven by mobility of the interstitial Li. We consider further the mobility of Li_i^{O+} below in relation to the spin-lattice relaxation.

Thus far, the ^{8}Li in ZnO follows the scenario typical for light implanted isotopes as outlined above. However, we also find clear evidence for another site (denoted C) with a well-defined EFG in the comb spectrum in Fig. 3(a). This site may correspond to a complex with another point defect, such as an oxygen vacancy, $Li_{Zn}-V_O$, which is Coulombically bound. This would be consistent with the high temperature appearance of the closely related $Na_{Zn}-V_O$ complex seen by electron-nuclear double resonance,[46] but the fact that the EFG for C is even smaller than B seems inconsistent with a nearby charged vacancy. Moreover, such a complex would have several orientations relative to the applied field which should yield a more complex spectrum. However, if the complex is *dynamic*, e.g. with V_O hopping rapidly (on the scale of the quadrupolar splitting of several kHz) among the three equivalent neighbours and axial position of Li_{Zn}^{-}, then a single reduced average EFG might result. This suggestion could be tested with more detailed calcula-tions.

Finally, we consider the *widths* of the well-resolved resonances. Without significant dipolar broadening, we might expect the resonances to be extremely narrow. However, the widths in Table I are considerably larger than similarly split satellites in crystals of Bi[58] or Sr_2RuO_4,[59] probably due to local crystalline disorder.[57] The primary broadening mechanism is quadrupolar, as confirmed by the substantially narrower MQ resonances. Another potential source of broadening is the inhomogeneous magnetic fields due to a population of dilute paramagnetic centres, which could be intrinsic defects[3] or impurities such as Fe. In NMR, this results in a term in the linewidth proportional to the impurity spin polarization that, in the dilute limit, is typically Curie-like (proportional to $1/T$). The absence of such a temperature dependent broadening is clear in Fig. 4(b), which shows the width to be quite independent of temperature below 150 K. The slight narrowing above this is probably related to the healing of nearby Frenkel pairs. This is consistent with predominantly quadrupolar broadening down to the lowest temperature. However, the MQ satellites, which are not quadrupole broadened, do exhibit a low T broadening (see Table I), suggesting a Curie term may be emerging at the lowest T. At the opposite end of the T range, the broadening at 370 K is probably dynamic, and we discuss it below with the spin-lattice relaxation.

B.   Magnetic State of Implanted ^{8}Li

In the previous section, we found very little evidence for broadening due to dilute paramagnetic defects. Here we consider paramagnetism in the immediate vicinity of the ^{8}Li. It is widely accepted that Li is an amphoteric dopant in ZnO, where the Li_i is a donor and Li_{Zn} an acceptor. The question then arises: what is the charge state? In the ionized state, both would be diamagnetic, while un-ionized they would be paramagnetic with an unpaired electron/hole spin localized in the vicinity. This distinction should be dramatic in the data, since the hyperfine interaction provides a strong magnetic perturbation on the NMR. However, we see no evidence for a hyperfine splitting for either site. This appears inconsistent with the EPR of Li_{Zn}.[60] However, the EPR signal requires cross gap photoexcitation of carriers, meaning it is actually due to a *metastable* paramagnetic defect. From our data, we conclude that Li_{Zn} is fully ionized in the temperature range where we observe it (above 200 K), meaning it is quite a shallow acceptor. Similarly, Li_i remains diamagnetic over the entire range down to the lowest T (7.6 K). Again this appears inconsistent with the EPR (and ENDOR) of the interstitial,[46] but this signal is observed (without photoexcitation) at 1.6 K, so it may be simply that ionization occurs in the intervening factor of 5 in T. However, this signal is also from nanoparticulate ZnO, and there is a strong size effect on the hyperfine coupling, due to confinement of the impu-

rity wavefunction, which decreases strongly with increasing particle size. At 7.6 K, we place an upper bound of a hyperfine splitting at 2 kHz (smaller than 3 Gauss at the ^{8}Li nucleus), corresponding to a fraction of the MQ linewidths in Table I, confirming that Li$_i$ is shallow as a donor in the bulk.

While the carrier concentration in our samples is quite low and far below the metallic limit, here we consider the possibility that the Li defects are un-ionized but rapidly exchanging with a population of free carriers. In this case, the hyperfine splitting is averaged out, but there is a remnant time average shift of the NMR which typically follows the Curie law.[61,62] The observed shift values in Table I show no evidence for such a contribution, remaining small (in the range of Li chemical shifts) at all temperatures. This provides further confirmation that the observed Li is fully ionized.

Fluctuations of the hyperfine field of an unpaired electron in the vicinity may well cause the ^{8}Li nuclear spin to relax so rapidly that it is not observed. This might account for the small missing fraction in the AG crystal. If this is the case, its reduction in the annealed crystal suggest that the probability of such a paramagnetic environment is reduced by annealing, i.e. it does not appear characteristic of pure ZnO.

C. Spin-Lattice Relaxation and Dynamics

Spin-lattice relaxation is driven by fluctuations of the local fields at the nucleus, specifically, the Fourier component at the NMR frequency (41.27 MHz). For quadrupolar nuclei, the most important contribution is usually EFG fluctuations, since this is the largest term in the nuclear spin Hamiltonian (after the Zeeman interaction with B_0). This hierarchy of interaction strengths is reflected in the time average spectra above, where the quadrupolar splitting far exceeds the satellite linewidths.

Below 300 K, the relaxation is so slow that it is difficult to measure reliably, due to lifetime of the probe. In this temperature range, thermal phonons could cause SLR by a Raman process, producing a $1/T_1$ varying approximately as T^2, e.g. in LaAlO$_3$, see Ref. 63. Such phonon relaxation is evidently too weak to measure.

In contrast, with an onset around 300 K, there is an activated increase in the $1/T_1^{\mathrm{slow}}$ above room temperature. This could, in principle, be due to thermally excited carriers,[28] but the peak in $1/T_1^{\mathrm{slow}}$ in Fig. 6 is not consistent with this. Such a peak is typical of some stochastic motion, either of the probe ion itself or some other species in its vicinity, giving rise to a fluctuating field at the nucleus. In the simplest case of the isolated Li$_i^{\mathrm{O+}}$ hopping diffusively on the sublattice of octahedral sites, the EFG at each site is equivalent, both in magnitude and direction, so fluctuations would occur only as the ion briefly transits between sites. On the other hand, the fluctuating EFG may be due to another nearby interstitial ion, probably the more mobile Zn$_I$, which is likely part of

the nearest Frenkel pair. If the corresponding vacancy remains nearby, then the dynamics of both interstitial cations would be modified by the Coulomb potential well of the negatively charged vacancy. The $1/T_1^{\mathrm{slow}}$ maximum may then correspond to a Bloembergen Purcell Pound (BPP) peak,[64] where a fluctuating field described by a single exponential correlation time τ_c with an activated temperature dependence $\tau_0\exp(E_a/k_bT)$ sweeps through the NMR frequency, producing a peak when τ_c matches ω_0^{-1}. Fitting the measured $1/T_1$ to the BPP model produces the curve shown in Fig. 6 with fitted values of $E_a = 0.57(2)$ eV and $\tau_0 = 3(1)\cdot 10^{-16}$ s. While the fit is not too bad, there are several important features that are inconsistent with a simple BPP interpretation: 1) The fitted "attempt frequency" $1/\tau_0$ is several orders of magnitude higher than expected. This value is related to the narrowness of the peak in temperature. 2) The SLR peak coincides with a *broadening* in the resonances (see Fig. 4). In contrast, the spectrum should be motionally narrowed when τ_c^{-1} exceeds the linewidth (several orders of magnitude smaller than ω_0), i.e. at temperatures well below the SLR peak. 3) Taking the A site ν_q as the scale of fluctuations, the peak value of $1/T_1$ is also too low. These inconsistencies suggest a more complicated situation than simple isolated interstitial diffusive motion.

For this reason, we seek an alternate explanation. Consider the line broadening at high temperature. It is not magnetic as the MQ resonances are unaffected. Rather it resembles the broadening expected for an NMR probe fluctuating between different environments at a frequency comparable to the spectral difference of the two. The width is maximized simultaneously for both the A and B lines as well as the broad background in the comb spectra. From this we speculate that some activated local dynamics starts to relax the ^{8}Li spin above 300 K, but before reaching the BPP peak, this relaxation channel is quenched. This might be Li$_i^{\mathrm{O+}}$ becoming mobile and then finding a vacancy and becoming the immobile Li$_{\mathrm{Zn}}^-$. On the other hand, it could also be Zn$_I$ beginning to hop locally in the attractive potential of the vacancy, and then detrapping and moving away. In either case, the activated dynamics is interrupted and the relaxation diminishes as this timescale becomes short enough to stop the relaxation.

D. Temperature Dependence of the EFG

The electric field gradient at the nucleus is sensitively determined by the site symmetry and the local electronic structure about the implanted ion. It is not surprising then to find that it is temperature dependent. For the A site, it decreases by more than 10% from its low T value to 400 K, see Fig. 2. The corresponding values of $V_{zz}(T)$ shown in Fig. 4(c) were fit to

$$V_{zz}(T) = V_{zz}(0)(1 - BT^\alpha). \qquad (6)$$

TABLE IV. Fit Parameters from Eq. (6) for the temperature dependence of the EFG at the Li$^+$ A site in ZnO. $V_{zz}(0)$ is in units of 10^{20}V/m^2.

Fit type	$V_{zz}(0)$	$B(\alpha)$	α
Fixed α	1.4507(2)	$1.47(2) \times 10^{-5}$	1.5
Free α	1.4428(3)	$4.4(2) \times 10^{-6}$	1.697(6)

The resulting parameters are reported in Table IV, where a $T^{1.7}$ behavior is determined for an unconstrained fit, while fixing $\alpha = 1.5$ produces a slightly worse fit with small deviations below 100 K.

It is widely recognized that thermal expansion plays only a minor role in determining $V_{zz}(T)$.[65] Instead, population of phonon modes renders the EFG time dependent, and the time average value is reduced as the vibrational amplitude increases,[66,67] resulting in an average behavior captured by the simple phenomenological form of Eq. (6), in a similar vein to the temperature dependence of the energy gap in semiconductors.[68] The exponent α is often found to be 3/2 for implanted defects in non-cubic metals and metallic compounds,[69] but, while common, it is by no means universal.[66] It's occurrence here demonstrates that it is not particular to metals[69,70] or narrow gap semiconductors,[71] nor is it characteristic of heavy isotope perturbed angular correlation probes. It would be a strong confirmation of the *ab initio* models, if lattice dynamic calculations[66,67] could reproduce the observed $V_{zz}(T)$.

In contrast, site B exhibits an anomalously increasing EFG, which, while rare, is not unheard of.[67] However, this should be interpreted with some caution, because the dynamic broadening at 370 K may also affect the apparent ν_q of the resonances. Confirmation of this behavior must await more detailed future measurements.

V. SUMMARY

Using ion-implanted ^{8}Li β-NMR we characterized the microscopic dynamics, stability, and magnetic states of Li defects in high purity ZnO single crystals. RF comb measurements, through a strong signal enhancement, enabled identification of three distinct defects between 7.6 and 400 K. Comparison to DFT calculations confirm the stability of ionized shallow donor Li$_i^{O+}$ up to 400 K and coexistence with Li$_{Zn}^-$ confirming the amphoteric character responsible for self-compensation of p-type doping. From the absence of a resonance shift or hyperfine splitting, we find no evidence for localized holes near Li$_{Zn}$ down to 210 K, indicating it is a shallow acceptor in isolated form. Above 370 K, a third unexpected defect is detected that we tentatively suggest to be a complex with Li$_{Zn}^-$. From spin-lattice relaxation measurements, a T independent fraction of the initial polarization suggest some ^{8}Li stop near magnetic defects with unpaired electrons that are reduced in concentration by annealing. The spin-lattice relaxation rate peaks at 370 K. We ascribe its temperature dependence to the coupled motional dynamics of Li and other nearby defects.

Our results using ultradilute ^{8}Li reveal the defect properties of Li in ZnO and indicate while p-type doping is possible with Li, self-compensation by interstitial Li poses a barrier. Characterization of the local ^{8}Li environment is a first step toward studies on surface properties, intentionally doped crystals, and the structurally related but more complex thin-film transistor material, IGZO. Finally, our measurements of $V_{zz}(T)$ for Li$_i$ demonstrating a $T^{1.7}$ dependence resembling a non-cubic metal provides a case to validate the *ab initio* lattice dynamics models for a light interstitial in a semiconductor.[66,67]

Appendix A: The Fast Relaxing Component

As discussed above, we fit the spin-lattice relaxation data to a biexponential relaxation function. Over much of the temperature range, the fast component ($f_f = 1 - f_s$) is small, accounting for only a few percent of the signal. As a result, it is much less well-determined than the larger slow relaxing component. For this reason, we did not discuss it in the main text. We include it here for completeness. Fig. 8 shows its rate and fraction.

For a spin-2 nucleus relaxing by slow quadrupolar fluctuations, one expects a biexponential with a fast component of about this amplitude.[72] However, the observed signal deviates from this model in several significant ways: 1) λ_f is substantially faster relative to λ_s than predicted; 2) $\lambda_f(T)$ should track $\lambda_s(T)$, while Fig. 8 shows that the main peak is substantially lower in temperature, and there is a secondary peak around 100 K; 3) When the fluctuations become fast, above the T_1 minimum, the fast amplitude should go smoothly to zero. Instead, it grows in this region. For these reasons, the fast component probably has a different origin. Below 350 K, where its amplitude is small, it may correspond to ^{8}Li in some exceptional environment with a significantly higher local relaxation rate, perhaps near the surface, but more measurements are required to make any firm conclusions.
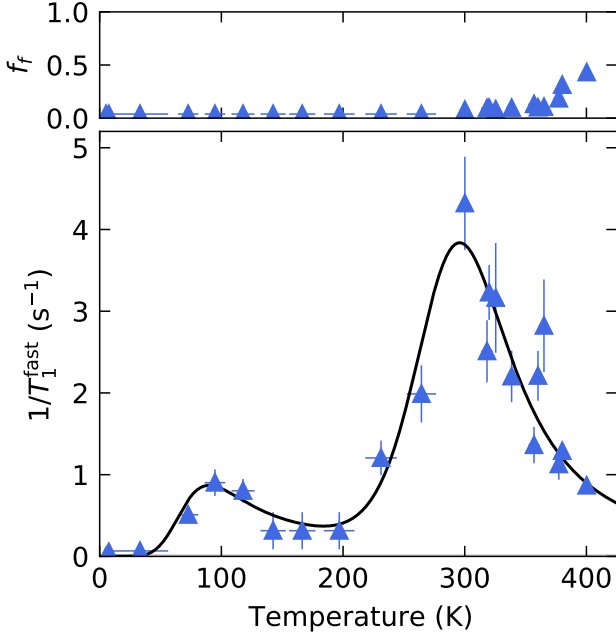
FIG. 8. The fast component's spin-lattice relaxation rate, $1/T_1^{\text{fast}}$ from biexponential fits to the data as shown in Fig. 8 at 6.55 T ∥ c. The peak occurs at about 300 K, significantly lower than the slow component.

FIG. 9. SRIM[18] stopping profile for 25 keV ^{8}Li$^+$ implanted in ZnO.

Appendix B: Stopping Distribution

The energy of the ^{8}Li$^+$ beam determines its implantation profile. We simulated this for 25 keV and 10^5 ions normally incident on ZnO with the SRIM Monte Carlo code, calculating a mean depth of 112.7 nm and a straggle (standard deviation) of 50.8 nm. The stopping distribution is shown in Fig. 9, indicating that the vast majority of ^{8}Li$^+$ are well beyond the surface region where the electronic properties are modified ($\sim$ 2 nm).[73] The simulation does not take into account implantation channeling which would result in a tail to the profile towards larger depths due to the channeled fraction.

Appendix D: Spin-Lattice Relaxation of the Annealed Crystal

In Fig. 11 we present a comparison of the NMR recovery curves at 300 K in annealed ZnO, as-grown ZnO, and

Appendix C: Helicity-Resolved Resonance Spectra

In Figure 10, we present the single tone RF spectrum at 300 K, separately for the two helicities. The occurrence of corresponding satellites on opposite sides of the centre of the pattern in the two helicities is unambiguous confirmation that the splittings are quadrupolar. The corresponding helicity combined spectrum is shown in Fig. 1.
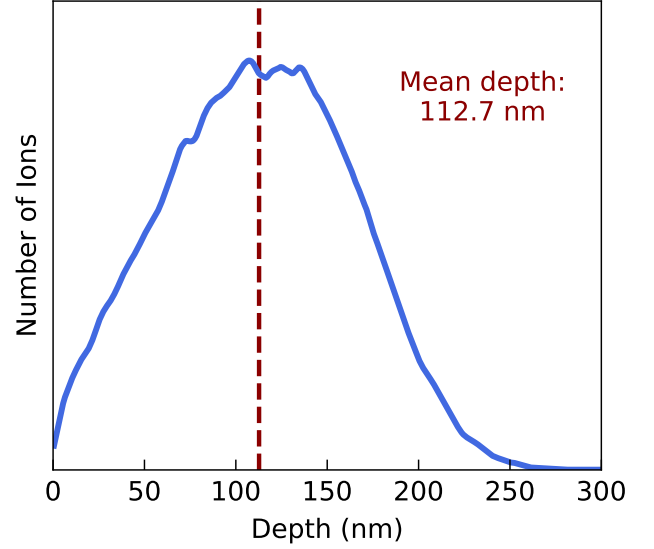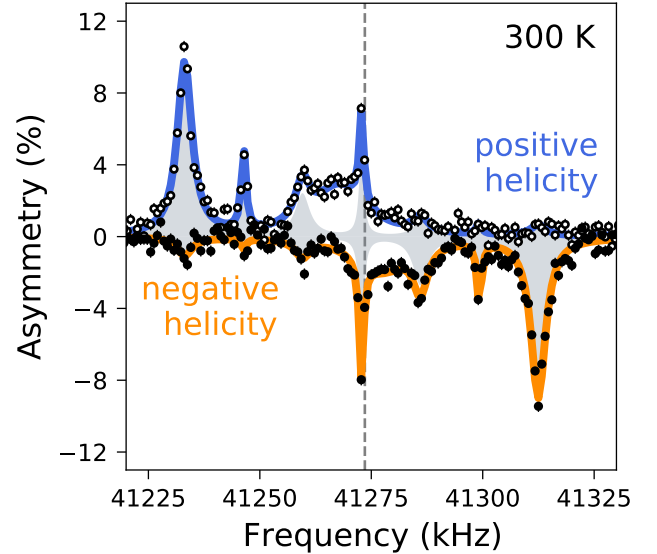

FIG. 10. The single RF spectra for ^{8}Li in the as-grown ZnO with 6.55 T∥ c at 300 K showing the two helicities: initial spin state primarily $m = 2$ (open) and $m = -2$ (closed). The asymmetry is normalized to its off-resonance equilibrium value. The site A spectrum is shaded grey.

the MgO reference. Using Eq. (5)[27] to fit the data, the initial asymmetry A_0 is extracted for n^+ ZnO and MgO. For MgO $A_0 = 0.095(1)$, while n^+ ZnO measured with the standard forward β detector yielded $A_0 = 0.0864(8)$.
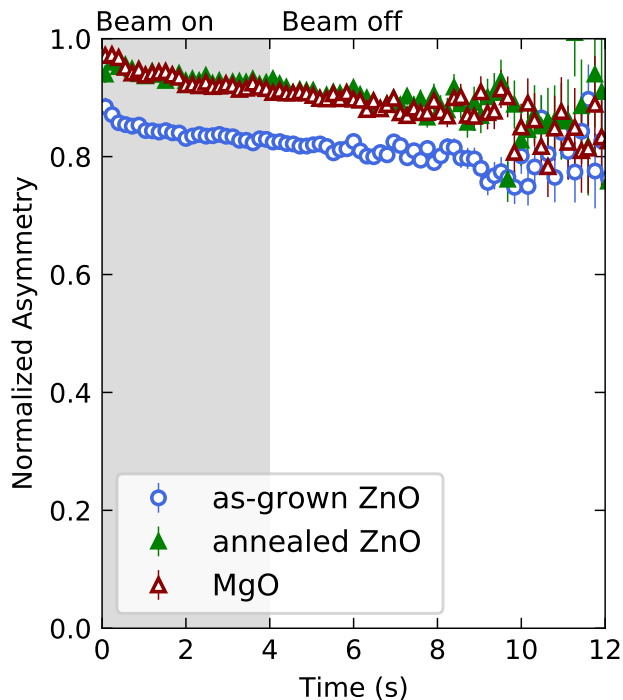

FIG. 11. The time dependence of the asymmetry for ^{8}Li$^+$ in the as grown ZnO, annealed ZnO, and MgO reference at 300 K and 6.55 Tesla$\parallel c$. The decay is due to spin-lattice relaxation of the isolated implanted ^{8}Li$^+$. The asymmetry is normalized to the initial asymmetry A_0 in MgO extracted from fitting a biexponential relaxation function. The as grown ZnO has a large reduction in the initial asymmetry, corresponding to a missing fraction.

REFERENCES

[*] Email: jradelman@berkeley.edu; Current address: Department of Chemistry, University of California, Berkeley, CA 94720, USA

[†] Current address: TRIUMF, 4004 Wesbrook Mall, Vancouver, BC V6T 2A3, Canada

[‡] Email: wam@chem.ubc.ca

[1] A. Janotti and C. G Van de Walle, Rep. Prog. Phys. **72**, 126501 (2009).

[2] D. C. Look, Mater. Sci. Eng., B **80**, 383 (2001).

[3] P. D. Esquinazi, W. Hergert, M. Stiller, L. Botsch, H. Ohldag, D. Spemann, M. Hoffmann, W. A. Adeagbo, A. Chassé, S. K. Nayak, and H. Ben Hamed, Phys. Status Solidi B **257**, 1900623 (2020).

[4] P. Sharma, A. Gupta, K. V. Rao, F. J. Owens, R. Sharma, R. Ahuja, J. M. O. Guillen, B. Johansson, and G. A. Gehring, Nat. Mater. **2**, 673 (2003).

[5] L. Botsch, I. Lorite, Y. Kumar, P. D. Esquinazi, J. Zajadacz, and K. Zimmer, ACS Appl. Electron. Mater. **1**, 1832 (2019).

[6] R. Gurwitz, R. Cohen, and I. Shalish, J. Appl. Phys. **115**, 033701 (2014).

[7] L. Gierster, S. Vempati, and J. Stähler, Nat. Commun. **12**, 978 (2021).

[8] M. D. McCluskey and S. J. Jokela, J. Appl. Phys. **106**, 071101 (2009).

[9] U. Özgür, Y. I. Alivov, C. Liu, A. Teke, M. A. Reshchikov, S. Doğan, V. Avrutin, S. J. Cho, and H. Morkoç, J. Appl. Phys. **98**, 041301 (2005).

[10] F. Rahman, Opt. Eng. **58**, 010901 (2019).

[11] J. Falson and M. Kawasaki, Rep. Prog. Phys. **81**, 056501 (2018).

[12] W. A. MacFarlane, Solid State Nucl. Magn. Reson. **68-69**, 1 (2015).

[13] K. Shimomura, K. Nishiyama, and R. Kadono, Phys. Rev. Lett. **89**, 255505 (2002).

[14] S. F. J. Cox, E. A. Davis, S. P. Cottrell, P. J. C. King, J. S. Lord, J. M. Gil, H. V. Alberto, R. C. Vilão, J. Piroto Duarte, N. Ayres de Campos, A. Weidinger, R. L. Lichti, and S. J. C. Irvine, Phys. Rev. Lett. **86**, 2601 (2001).

[15] B. Ittermann, M. Füllgrabe, M. Heemeier, F. Kroll, F. Mai, K. Marbach, P. Meier, D. Peters, G. Welker, W. Geithner, S. Kappertz, S. Wilbert, R. Neugart, P. Lievens, U. Georg, and M. Keim, Hyperfine Interact. **129**, 423 (2000).

[16] B. Ittermann, G. Welker, F. Kroll, F. Mai, K. Marbach, and D. Peters, Phys. Rev. B **59**, 2700 (1999).

[17] K. Nomura, H. Ohta, A. Takagi, T. Kamiya, M. Hirano, and H. Hosono, Nature **432**, 488 (2004).

[18] J. F. Ziegler, M. D. Ziegler, and J. P. Biersack, Nucl. Instrum. Methods Phys. Res., Sect. B **268**, 1818 (2010).

[19] C. D. P. Levy, M. R. Pearson, R. F. Kiefl, E. Mané, G. D. Morris, and A. Voss, Hyperfine Interact. **225**, 165 (2014).

[20] A. Voss, M. R. Pearson, J. Billowes, F. Buchinger, K. H. Chow, J. E. Crawford, M. D. Hossein, R. F. Kiefl, C. D. P. Levy, W. A. MacFarlane, E. Mané, G. D. Morris, T. J. Parolin, H. Saadaoui, Z. Salman, et al., J. Phys. G: Nucl. Part. Phys. **38**, 075102 (2011).

[21] A. J. Vega, "Quadrupolar nuclei in solids," in eMagRes, edited by R. K. Harris and R. L. Wasylishen (Wiley Inter-Science, New York, 2010).

[22] S. Vega, T. W. Shattuck, and A. Pines, Phys. Rev. Lett. **37**, 43 (1976).

[23] P. Blaha, K. Schwarz, and P. Herzig, Phys. Rev. Lett. **54**, 1192 (1985).

[24] K. Schwarz, C. Ambrosch-Draxl, and P. Blaha, Phys. Rev. B **42**, 2051 (1990).

[25] P. Blaha, K. Schwarz, and P. H. Dederichs, Phys. Rev. B **37**, 2792 (1988).

[26] G. N. Darriba, R. Faccio, and M. Rentería, Phys. Rev. B **99**, 195435 (2019).

[27] W. A. MacFarlane, T. J. Parolin, D. L. Cortie, K. H. Chow, M. D. Hossain, R. F. Kiefl, C. D. P. Levy, R. M. L. McFadden, G. D. Morris, M. R. Pearson, H. Saadaoui, Z. Salman, Q. Song, and D. Wang, J. Phys. Conf. Ser. **551**, 012033 (2014).

[28] H. Selbach, O. Kanert, and D. Wolf, Phys. Rev. B **19**, 4435 (1979).

[29] K. Maeda, M. Sato, I. Niikura, and T. Fukuda, Semicond. Sci. Technol. **20**, S49 (2005).

[30] K. Minamisono, K. Matsuta, T. Minamisono, C. D. P. Levy, T. Nagatomo, M. Ogura, T. Sumikama, J. A. Behr, K. P. Jackson, M. Mihara, and M. Fukuda, Nucl. Instrum. Methods Phys. Res., Sect. A **616**, 45 (2010).

[31] T. Minamisono, T. Ohtsubo, S. Fukuda, I. Minami, Y. Nakayama, M. Fukuda, K. Matsuta, and Y. Nojiri, Hyperfine Interact. **80**, 1315 (1993).

[32] S. Lany, P. Blaha, J. Hamann, V. Ostheimer, H. Wolf, and T. Wichert, Phys. Rev. B **62**, R2259 (2000).

[33] T. Wichert and S. Lany, Hyperfine Interact. **136**, 453 (2001).

[34] P. Giannozzi, O. Andreussi, T. Brumme, O. Bunau, M. B. Nardelli, M. Calandra, R. Car, C. Cavazzoni, D. Ceresoli, M. Cococcioni, N. Colonna, I. Carnimeo, A. D. Corso, S. de Gironcoli, P. Delugas, *et al.*, J. Phys.: Condens. Matter **29**, 465901 (2017).

[35] N. Troullier and J. L. Martins, Phys. Rev. B **43**, 1993 (1991).

[36] J. P. Perdew, K. Burke, and M. Ernzerhof, Phys. Rev. Lett. **77**, 3865 (1996).

[37] H. J. Monkhorst and J. D. Pack, Phys. Rev. B **13**, 5188 (1976).

[38] R. R. Reeber, J. Appl. Phys. **41**, 5063 (1970).

[39] P. Blaha, K. Schwarz, F. Tran, R. Laskowski, G. K. H. Madsen, and L. D. Marks, J. Chem. Phys. **152**, 074101 (2020).

[40] W. A. MacFarlane, G. D. Morris, K. H. Chow, R. A. Baartman, S. Daviel, S. R. Dunsiger, A. Hatakeyama, S. R. Kreitzman, C. D. P. Levy, R. I. Miller, K. M. Nichol, R. Poutissou, E. Dumont, L. H. Greene, and R. F. Kiefl, Physica B **326**, 209 (2003).

[41] F. James and M. Roos, Comput. Phys. Commun. **10**, 343 (1975).

[42] M. Hatlo, F. James, P. Mato, L. Moneta, M. Winkler, and A. Zsenei, IEEE Trans. Nucl. Sci. **52**, 2818 (2005).

[43] H. Mikhail and F. I. Agami, J. Phys. Chem. Solids **27**, 909 (1966).

[44] R. Brun and F. Rademakers, Nucl. Instrum. Methods Phys. Res., Sect. A **389**, 81 (1997).

[45] C. Freysoldt, B. Grabowski, T. Hickel, J. Neugebauer, G. Kresse, A. Janotti, and C. G. Van de Walle, Rev. Mod. Phys. **86**, 253 (2014).

[46] S. B. Orlinskii, J. Schmidt, P. G. Baranov, D. M. Hofmann, C. de Mello Donegá, and A. Meijerink, Phys. Rev. Lett. **92**, 047603 (2004).

[47] A. Carvalho, A. Alkauskas, A. Pasquarello, A. K. Tagantsev, and N. Setter, Phys. Rev. B **80**, 195205 (2009).

[48] R. Vidya, P. Ravindran, and H. Fjellvåg, J. Appl. Phys. **111**, 123713 (2012).

[49] K. Momma and F. Izumi, J. Appl. Crystallogr. **44**, 1272 (2011).

[50] E. Rimini, "Radiation damage," in *Ion Implantation: Basics to Device Fabrication* (Springer US, Boston, 1995) pp. 131–172.

[51] U. Wahl, J. G. Correia, L. Amorim, S. Decoster, M. R. da Silva, and L. M. C. Pereira, Semicond. Sci. Technol. **31**, 095005 (2016).

[52] U. Wahl, L. M. Amorim, V. Augustyns, A. Costa, E. David-Bosne, T. A. L. Lima, G. Lippertz, J. G. Correia, M. R. da Silva, M. J. Kappers, K. Temst, A. Vantomme, and L. M. C. Pereira, Phys. Rev. Lett. **118**, 095501 (2017).

[53] U. Wahl, E. David-Bosne, L. M. Amorim, A. R. G. Costa, B. De Vries, J. G. Correia, M. R. da Silva, L. M. C. Pereira, and A. Vantomme, J. Appl. Phys. **128**, 045703 (2020).

[54] L. S. Vlasenko and G. D. Watkins, Phys. Rev. B **72**, 035203 (2005).

[55] K. E. Knutsen, K. M. Johansen, P. T. Neuvonen, B. G. Svensson, and A. Y. Kuznetsov, J. Appl. Phys. **113**, 023702 (2013).

[56] G. D. Morris, W. A. MacFarlane, K. H. Chow, Z. Salman, D. J. Arseneau, S. Daviel, A. Hatakeyama, S. R. Kreitzman, C. D. P. Levy, R. Poutissou, R. H. Heffner, J. E. Elenewski, L. H. Greene, and R. F. Kiefl, Phys. Rev. Lett. **93**, 157601 (2004).

[57] A. Janotti and C. G. Van de Walle, Phys. Rev. B **76**, 165202 (2007).

[58] W. A. MacFarlane, C. B. L. Tschense, T. Buck, K. H. Chow, D. L. Cortie, A. N. Hariwal, R. F. Kiefl, D. Koumoulis, C. D. P. Levy, I. McKenzie, F. H. McGee, G. D. Morris, M. R. Pearson, Q. Song, D. Wang, *et al.*, Phys. Rev. B **90**, 214422 (2014).

[59] D. L. Cortie, T. Buck, M. H. Dehn, R. F. Kiefl, C. D. P. Levy, R. M. L. McFadden, G. D. Morris, M. R. Pearson, Z. Salman, Y. Maeno, and W. A. MacFarlane, Phys. Rev. B **91**, 241113 (2015).

[60] O. Schirmer, J. Phys. Chem. Solids **29**, 1407 (1968).

[61] E. M. Meintjes, J. Danielson, and W. W. Warren, Phys. Rev. B **71**, 035114 (2005).

[62] K. H. Chow, R. F. Kiefl, B. Hitti, T. L. Estle, and R. L. Lichti, Phys. Rev. Lett. **84**, 2251 (2000).

[63] V. L. Karner, R. M. L. McFadden, A. Chatzichristos, G. D. Morris, M. R. Pearson, C. D. P. Levy, Z. Salman, D. L. Cortie, R. F. Kiefl, and W. A. MacFarlane, JPS Conf. Proc. **21**, 011023 (2018).

[64] N. Bloembergen, E. M. Purcell, and R. V. Pound, Phys. Rev. **73**, 679 (1948).

[65] P. Raghavan, E. N. Kaufmann, R. S. Raghavan, E. J. Ansaldo, and R. A. Naumann, Phys. Rev. B **13**, 2835 (1976).

[66] D. Torumba, K. Parlinski, M. Rots, and S. Cottenier, Phys. Rev. B **74**, 144304 (2006).

[67] A. V. Nikolaev, N. M. Chtchelkatchev, D. A. Salamatin, and A. V. Tsvyashchenko, Phys. Rev. B **101**, 064310 (2020).

[68] K. P. O'Donnell and X. Chen, Appl. Phys. Lett. **58**, 2924 (1991).

[69] J. Christiansen, P. Heubes, R. Keitel, W. Klinger, W. Loeffler, W. Sandner, and W. Witthuhn, Z. Phys. B **24**, 177 (1976).

[70] K. Nishiyama, F. Dimmling, T. Kornrumpf, and D. Riegel, Phys. Rev. Lett. **37**, 357 (1976).

[71] L. Amaral, M. Behar, A. Maciel, and H. Saitovitch, Phys. Lett. A **102**, 45 (1984).

[72] K. D. Becker, Z. Naturforsch. A **37**, 697 (1982).

[73] J.-C. Deinert, O. T. Hofmann, M. Meyer, P. Rinke, and J. Stähler, Phys. Rev. B **91**, 235313 (2015).